# Characterisation and disposability assessment of multi-waste stream in-container vitrified products for higher activity radioactive waste

Sam A. Walling, Marcus N. Kauffmann, Laura J. Gardner, Daniel J. Bailey, Martin C. Stennett, Claire L. Corkhill, Neil C. Hyatt *

*Immobilisation Science Laboratory, Department of Materials Science & Engineering, The University of Sheffield, Sheffield, S1 3JD, United Kingdom*

## ARTICLE INFO

## ABSTRACT

Materials from GeoMelt® In-Container Vitrification (ICV)™ of simulant UK nuclear wastes were characterised to understand the partitioning of elements, including inactive surrogates for radionuclide species of interest, within the heterogeneous products. Aqueous durability analysis was performed to assess the potential disposability of the resulting wasteforms. The vitrification trial aimed to immobilise a variety of simulant legacy waste streams representative of decommissioning operations in the UK, including plutonium contaminated material, Magnox sludges and ion-exchange materials, which were vitrified upon the addition of glass forming additives. Two trials with different wastes were characterised, with the resultant vitreous wasteforms comprising olivine and pyroxene crystalline minerals within glassy matrices. Plutonium surrogate elements were immobilised within the glassy fraction rather than partitioning into crystalline phases. All vitrified products exhibited comparable or improved durability to existing UK high level waste vitrified nuclear wasteforms over a 28 day period.

## 1. Introduction

Radioactive wastes arising from current and legacy nuclear fuel cycle operations pose a significant decommissioning challenge to the UK due to the volume and complexity of the wastes. Although suitable management and disposal routes exist and are being implemented for certain wastes, many higher activity materials remain in storage with unclear or undecided solutions.

Higher activity radioactive wastes in the UK include some irradiated nuclear fuels and highly active liquors from reprocessing. This category also includes larger volume, moderate activity intermediate level wastes (ILW) such as: sludges, flocs, activated metals, ion-exchange resins, and other miscellaneous materials (Nuclear Decommissioning Authority, 2016, 2019a). These typically arise due to fuel handling operations, site decommissioning, contact handling of plutonium, and operational activities. These are a highly diverse array of wastes with large volumes from legacy operations. Many of these ILW wastes are solidified *via* cementation, which has long been a default waste treatment option in the UK. Large scale cementation operations began with Magnox swarf wastes in 1990, expanding to several cementation plants and a more diverse range of wastes treated over succeeding years at Sellafield, Dounreay and the LLWR (Fenton and Holland, 2001; Fairhall and

Palmer, 1992). Although cementation has become the baseline waste treatment strategy, cement encapsulation of ILW results in an increase of the packaged waste volume, and adverse reactions may arise with certain wastes such as reactive metals or ion-exchange resins (Sharp et al., 2003; Cronin and Collier, 2011; Utton and Godfrey, 2010). This has driven research, both in the UK and internationally, towards expanding vitrification or other thermal treatment technologies for ILW waste streams as an option within a toolkit of immobilisation technologies (Radioactive Waste Management (RWM), 2017; Bennett et al., 2001).

Thermal treatment has the potential for waste volume reduction, destruction of organic materials, passivation of reactive metals and removal of water from wastes (Radioactive Waste Management (RWM), 2017), which are problematic characteristics of some UK ILW wastes. Large volumes of these wastes currently exist in the UK without a final treatment route decided, for which thermal treatment could form a credible solution, such as: Magnox fuel, sludges, plutonium contaminated material, Pile fuel cladding material and miscellaneous beta-gamma wastes (Nuclear Decommissioning Authority, 2015).

Currently, thermal treatment is the baseline technology for the immobilisation of highly active liquors from reprocessing operations, with calcined liquor and glass frit melted to form a solid, vitreous

product, with full scale waste vitrification operations at Sellafield since 1989 (Dunnett, 2007; Bradshaw et al., 2007). Worldwide, vitrification of radioactive wastes is a well-established principle which is a cornerstone of waste treatment in many countries. Several broad categories of technology are, or have been in operation, including: hot wall induction melting (France, UK), in-pot / batch induction melting (India, Slovakia), and joule heated melting (USA, Belgium, Germany, Russia, Japan, India) (Gin et al., 2013; Jantzen and Ojovan, 2019; Vienna, 2010).

These facilities have usually been constructed and operated for high-level waste vitrification, typically from current or historical nuclear fuel reprocessing operations, utilising a borosilicate or alumino-phosphate glass formulation (Jantzen and Ojovan, 2019; Robbins and Ojovan, 2016). Some lower activity waste vitrification facilities have, however, operated or are currently under construction. Such sites include the WVP at Hanford (USA) for processing of both higher and lower activity tank wastes (Kim, 2015; Hujova et al., 2020; Goel et al., 2019), LILW vitrification of dry active waste / ion exchange resins in the Republic of Korea (Kim et al., 2020), and some ILW vitrification in Russia (Jantzen and Ojovan, 2019; Ojovan and Lee, 2011; Laverov et al., 2013).

Development of lower activity waste vitrification is less technologically mature, principally as much lower activity waste is routed to other treatment options such as cementation, bituminisation or compaction and containerisation, along with complicated and varied chemistries (Bingham et al., 2012). Multiple technologies are, however, in varying stages of development or operation for lower activity wastes (contaminated soil, ion-exchange resins, etc.), often with the aim of volume reduction via thermal treatment. These include, but are not limited to; hot isostatic pressing to form glass/glass ceramics, in-can melting, plasma arc melting, thermal gasification of ion exchange resins, in-situ subsurface melting and microwave vitrification (Zhang et al., 2017; Shu et al., 2020; Scourfield et al., 2020; Nieminen et al., 2019).

Arguably the most mature technology is plasma torch melting at the Zwilag plasma facility in Switzerland, where low level radioactive waste is treated, to form a volume reduced slag material (Heep, 2011; Deckers, 2011). The UK itself has been advancing the development and implementation of hot-isostatic pressing (HIP) technology, as a credible solution for disposition of the UK plutonium stockpile and residues (Nuclear Decommissioning Authority, 2010; Thornber et al., 2018), with further research on immobilisation of ion exchange materials (Chen et al., 2018) and Magnox sludges (Heath et al., 2018). Another thermal treatment technology being trialled for use in the UK is in-container vitrification (ICV) based on joule heating within a refractory container. This enables the use of the vitrification vessel as a long-term storage container rather than requiring transfer to a disposal container, with the option to refractory line ISO freight containers as larger wasteforms (Radioactive Waste Management (RWM), 2017). Various trials have been undertaken using UK relevant wastes, and further inactive trials successfully produced melts for various problematic waste stream simulants (Witwer and Dysland, 2010; Campbell et al., 2016; Witwer et al., 2013).

In-container vitrification technology has been trialled for problematic wastes across the world. This includes in the USA for treatment of depleted uranium chips in soil (Finucane and Campbell, 2006), solidification of low activity wastes at Hanford (Witwer et al., 2008, 2006), and for the destruction of metallic sodium containing wastes (Garrett et al., 2020). In Japan, for treatment of chlorinated organics and contaminated soil (Thompson, 2002), along with destruction of asbestos (Finucane et al., 2008). Within the UK, this technology is continuing to gain interest for various active wastes, sludges and sea disposal containers (Campbell et al., 2017; Clarke et al., 2020). Considering the wide range of global applications, it is imperative that resultant products are well characterised to build confidence in this vitrification technology.

This paper characterises the resulting product from two trial melts using the GeoMelt In-Container Vitrification (ICV) technology (Witwer and Dysland, 2010), and are being characterised here as part of a larger EC-funded study on thermal treatment of radioactive wastes

**Table 1**
Trial 1 formulation (adapted from (Witwer and Dysland, 2010)).

| Simulant Component | Mass of Feed (kg) | % of Total |
|---|---|---|
| **Staged – PCM Simulant** | | |
| Carbon Steel Drum Fragments | 78.9 | 10.40 |
| Stainless Steel | 7.1 | 0.94 |
| Misch Metal (*Pu surrogate*) | 0.5 | 0.07 |
| PVC as gloves | 24.1 | 3.18 |
| Rubber | 9.7 | 1.28 |
| Polyethylene | 5.4 | 0.71 |
| Portland Cement | 18.7 | 2.46 |
| Cellulose, Bottle glass, Concrete | 27.0 | 3.56 |
| Local soil | 163.0 | 21.48 |
| **Subtotal** | **334** | **44.01** |
| | | |
| **FWM – SIXEP Magnox Sludge Simulant** | | |
| De-mineralized Water | 64.0 | 8.43 |
| Misch Metal | 2.9 | 0.38 |
| Brucite $Mg(OH)_2$ | 82.3 | 10.84 |
| Local soil | 276.3 | 36.40 |
| **Subtotal** | **425** | **55.99** |
| | | |
| **Final Total** | **759** | **100** |

**Table 2**
Trial 2 formulation (adapted from (Witwer and Dysland, 2010)).

| Simulant Component | Mass of Feed (kg) | % of Total |
|---|---|---|
| **Pile Fuel Cladding Silo Simulant** | | |
| C – Graphite | 13.5 | 3.31 |
| $CaCO_3$ – Limestone | 5.5 | 1.35 |
| Fe – Steel | 14.8 | 3.63 |
| Mg – metal (rods) | 16.0 | 3.93 |
| $Mg(OH)_2$ – brucite | 4.3 | 1.06 |
| $Al_2O_3$ – Alumina | 4.3 | 1.06 |
| Cellulose | 2.2 | 0.54 |
| Hydraulic Oil | 0.3 | 0.07 |
| **Subtotal** | **60.9** | **14.95** |
| | | |
| **SIXEP Sand/Clinoptilolite Simulant** | | |
| Demineralized Water | 34.1 | 8.37 |
| Clinoptilolite | 42.4 | 10.41 |
| Silica Sand | 10.5 | 2.58 |
| Misch Metal | 0.8 | 0.20 |
| $Mg(OH)_2$ – Brucite | 4.0 | 0.98 |
| $Al_2O_3$ – Alumina | 0.1 | 0.02 |
| CaO – Quicklime | 0.4 | 0.10 |
| $Fe_2O_3$ – Hematite | 0.1 | 0.02 |
| $Na_2CO_3$ – Sodium Carbonate | 0.2 | 0.05 |
| $K_2O$ – Potash | 0.2 | 0.05 |
| **Subtotal** | **92.8** | **22.78** |
| | | |
| Soil/Hematite Glass Forming Additives | 253.6 | 62.26 |
| **Final Total** | **407.3** | **100** |

(THERAMIN) (Nieminen et al., 2019). These melts were undertaken in 2009 at the GeoMelt Horn Rapids Test Site in Richland, WA, USA, simulating wastes from the UK Sellafield site at scale of ~400−750 kg melts.

Trial 1 was a simulated dual waste mix of plutonium contaminated material (PCM) and Magnox sludge, as detailed in Table 1. These are both larger volume problematic waste streams in the UK and are designated as Intermediate Level Waste (ILW) (Nuclear Decommissioning Authority, 2019a). PCM waste largely consists of PVC gloves, steel, rubber, filters, paper towels and other materials from Pu contact operations. There are several sources of these wastes, including from reprocessing operations (Nuclear Decommissioning Authority, 2019b), historical MOX fabrication (Nuclear Decommissioning Authority, 2019c), defence facilities (Nuclear Decommissioning Authority, 2019d, 2019e) and decommissioning Sellafield / Low Level Waste Repository (Nuclear Decommissioning Authority, 2019f), of which the latter alone is expected

to result in 48,740 m$^3$ waste over the next 100 years. The other waste, Magnox sludge, has largely resulted from historic degradation of Magnox fuel cladding in legacy ponds / silos across the Sellafield site. This material is largely Mg(OH)$_2$ with various U oxides, Al, cans / filters, tools, pipework, etc. dependant on sludge location (Nuclear Decommissioning Authority, 2019g, 2019h). The melt setup was an initial "bottom-up melt" plus "feed with melt" (FWM) to compensate for volume reduction (~30 %), with elemental tracers added to determine elemental partitioning between glass and metal fraction. The mass of feed and additives are shown in Table 1.

Trial 2 was also a dual-waste melt, however this utilised a "top-down" melting system where all of the material was added to the container before melting (Table 2). Simulated wastes were Pile fuel cladding silo, and SIXEP simulants. These are also UK-specific wastes, with Pile fuel cladding silo wastes largely arising from the early UK reactors Windscale, Calder Hall and Chapelcross along with early reprocessing in 1951–1965. This waste constitutes magnesium, aluminium and uranium metals, sludges, graphite, gravel, scrap steel and miscellaneous organic materials, which have been stored in a silo for ~60 years, with an estimated volume of 3231 m$^3$ (Nuclear Decommissioning Authority, 2019i). The second waste stream was Site Ion Exchange Plant (SIXEP) material, predominantly consisting of an inorganic aluminosilicate ion-exchange material (clinoptilolite) and sand used for treatment of liquid effluents on the Sellafield site. This is another high volume waste, with a current inventory of 1335 m$^3$, with volumes expected to rise to 2975 m$^3$ by 2060 (Nuclear Decommissioning Authority, 2019j). In addition to the components noted in Tables 1 & 2, both trials incorporated a quantity of Ce, Cs, Sr, Co, Re and Eu as tracers to determine elemental partitioning into the glass or off-gas system.

Successful incorporation of these wastes within a vitrified product could achieve notable cost savings compared to bulk cementation, or enable disposal of problematic wastestreams (Nieminen et al., 2019; Hyatt et al., 2014; Nuclear Decommissioning Authority, 2018). In the UK, cementation of ILW waste is estimated to result in an increased packaged volume (247,000 m$^3$ unpackaged ILW waste, rising to 499,000 m$^3$ once packaged (Nuclear Decommissioning Authority, 2019a)), as wastes are mixed within a cementitious binder increasing the overall volume. Waste volume is a key driver of cost of interim storage facilities, the cost of a geological disposal facility, and the cost of requisite radioactive waste transport. Interim storage is particularly relevant to the UK decommissioning programme, as construction of a geological disposal facility will not begin for at least a decade, entailing interim storage of treated and packaged wastes for several decades prior to disposal. The wastes chosen within this trial were particularly suitable for thermal treatment, since SIXEP sand / clinoptilolite are largely aluminosilicates, and act as useful glass forming materials. Magnox sludge contains a large



**Fig. 1.** Photograph of Trial 1 sample indicating sections of interest; A) dark region, B) light region, C) crystalline region.

volume of water and Mg(OH)$_2$, thermal processing of this will drive off water, and convert Mg(OH)$_2$ can to MgO, reducing the waste volume. Mg metal in these wastes can be passivated within a thermal system (Mg metal risks expansive corrosion within cement pore solution (Cronin and Collier, 2011; Setiadi et al., 2006)), incorporating as Mg within a glassy matrix. Oil and plastic materials will also be consumed during thermal treatment, affording a more homogeneous, stable product for disposal.

The aim of this study is to characterise the physical and chemical properties of these vitrified simulant ILW materials, and further our understanding of their aqueous durability, to improve confidence in alternative vitrification technologies for challenging wastes.

## 2. Experimental programme

### 2.1. Materials

Several solid samples were provided from both trials post-vitrification, undertaken in 2009 (Witwer and Dysland, 2010), with one representative piece of material selected from each melt, upon which further analysis was undertaken. Material from Trial 1 is from the bulk glass, while material from Trial 2 consists of a solidified foam atop the melt (representing a 'worst case' material for testing).

### 2.2. Analytical methods

X-ray diffraction patterns were collected using a Bruker D2 PHASER diffractometer (Cu Kα, 1.5418 Å), with a Ni filter, with data collected between $10° < 2θ < 60°$ using a 0.01° step size and a 1 s dwell time per step. Prior to data collection samples were crushed in an agate mortar and passed through a 63 μm sieve.

SEM analysis and elemental mapping was undertaken using a Hitachi TM3030 Scanning Electron Microscope, coupled with a Bruker Quantax 70 Energy Dispersive X-ray Spectrophotometer (EDX). Images were collected in backscattered electron mode using a 15 kV accelerating voltage. Samples were prepared by cutting a section of vitrified material using a diamond wafering blade, and embedding this in an epoxy resin stub. This was then ground using SiC grit paper using sequentially finer grit, then polished to a 1 μm finish using diamond suspension and finally carbon coated.

Durability assessment was performed following the ASTM C1285 methodology (the PCT-B protocol). Samples were crushed and sieved to 75–150 μm size fraction, and repeatedly washed with isopropanol (Sigma-Aldrich, ACS reag. ≥ 99.8 % (GC)) to remove fines. Pre-cleaned PFA vessels were used, filled with ASTM Type 1 water and glass was added to achieve a surface area to volume ratio (SA/V) of 1200 m$^{-1}$ (by geometric surface area, density *via* helium pycnometry (Micrometrics Accupyc II)). Vessels were stored at 90 ± 3 °C, with duplicate vessels and blanks (no glass added) removed for sampling at each time point (1, 3, 7, 14, 21 and 28 days). The resulting leachate was filtered using 0.2 μm cellulose acetate syringe filters, pH measured at room temperature, then acidified using high purity nitric acid (VWR, Ultrapure NORMATOM, 67–69 % HNO$_3$). Acidified samples were analysed for elemental concentrations in solution using by ICP-OES (Thermo-Fisher 6000 iCAP Duo) for Si, Al, Na, Ca, Mg and Sr, or ICP-MS (Thermo Scientific iCAP RQ) for Ce, Cr and Nd, with resulting data normalised to geometric surface area and sample elemental composition determined by XRF analysis (PANalytical PW2404).

XAS data, to ascertain the oxidation state of the Pu surrogate, Ce, were acquired on the beam line B18 at Diamond Light Source, Harwell, UK. Beamline B18 utilises a collimating mirror, a fixed-exit double crystal Si(111) monochromator and a double toroidal focussing mirror. Ce L$_3$-edge XAS data were acquired on B18 in fluorescence mode using finely ground specimens dispersed in polyethylene glycol and pressed as a pellet, oriented at 45° to the incident X-ray beam and detector. Incident and transmitted beam intensities were measured using ionization chambers, filled with mixtures of He and N$_2$, operated in a stable region
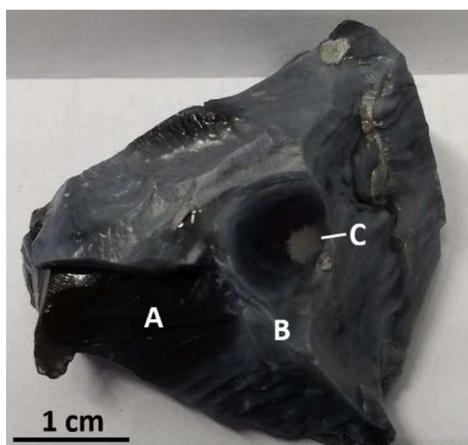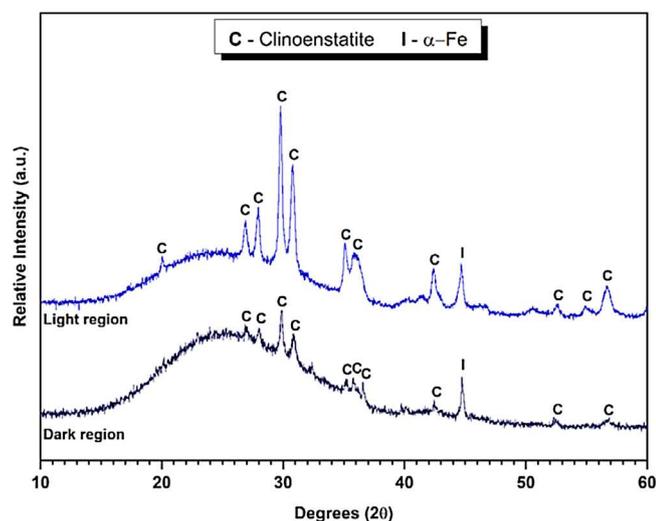
**Fig. 2.** X-ray diffraction patterns for Trial 1.



**Fig. 3.** Backscattered electron micrograph and elemental maps of the dark region (A) in Trial 1.

**Table 3**
XRF composition of both trial bulk glassy materials (error ± 5% of stated value).

| Oxide | Trial 1 | | Trial 2 | |
|---|---|---|---|---|
| | (wt. %) | (mol. %) | (wt. %) | (mol. %) |
| $Al_2O_3$ | 12.68 | 7.54 | 7.39 | 4.79 |
| CaO | 5.47 | 5.91 | 2.70 | 3.18 |
| $Ce_2O_3$ | 0.26 | 0.05 | 0.15 | 0.03 |
| $Cr_2O_3$ | 0.06 | 0.02 | 0.04 | 0.02 |
| $Fe_2O_3$ | 0.65 | 0.25 | 17.52 | 7.25 |
| $K_2O$ | 1.38 | 0.89 | 1.27 | 0.89 |
| $La_2O_3$ | 0.26 | 0.05 | 0.14 | 0.03 |
| MgO | 12.03 | 18.10 | 11.68 | 19.13 |
| $Mn_3O_4$ | 0.24 | 0.06 | 0.16 | 0.05 |
| $Na_2O$ | 5.98 | 5.85 | 1.25 | 1.33 |
| $Nd_2O_3$ | n.d.* | n.d.* | n.d.* | n.d.* |
| $SiO_2$ | 60.05 | 60.58 | 57.29 | 62.97 |
| SrO | 0.05 | 0.03 | 0.03 | 0.02 |
| $TiO_2$ | 0.90 | 0.69 | 0.39 | 0.32 |

* $Nd_2O_3$ not detected, however may be present depending on added misch metal composition, and any overlapping X-ray fluorescence intensities complicating peak assignment for XRF data.

of their I/V curve. Fluorescence emission was detected using a four channel Si-drift detector, with appropriate dead time correction. A chromium foil was used as an internal energy calibration where the first inflection point was defined to be 5959.2 eV. Data reduction and analysis was performed using the programmes Athena, Artemis and Hephaestus (Ravel and Newville, 2005).

## 3. Results and discussion

### 3.1. Trial 1 - composition and characteristics

The sample provided from Trial 1 (PCM-Magnox simulant) constituted several pieces of heterogeneous glassy material, of which the analysed sample is shown in Fig. 1. The material was visually glassy, but exhibited clear heterogeneities; as such, for further analysis, the material was divided into three sections of interest: a) dark region, b) light region, c) crystalline region. Both the light and dark region XRD patterns are displayed in Fig. 2, revealing a largely glassy material with reflections identified as clinoenstatite ($MgSiO_3$) and alpha iron. The intensity of these reflections was more pronounced in the light region. Not enough pure material from region C – 'crystalline region' was able to be collected and prepared for XRD analysis, however more detailed SEM analysis was undertaken on this region to determine the elemental
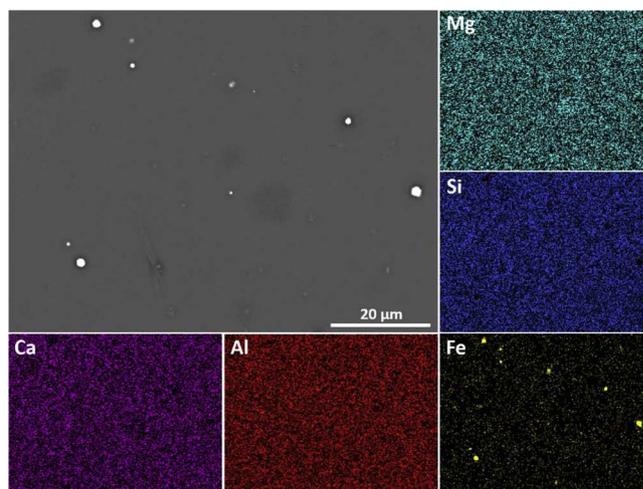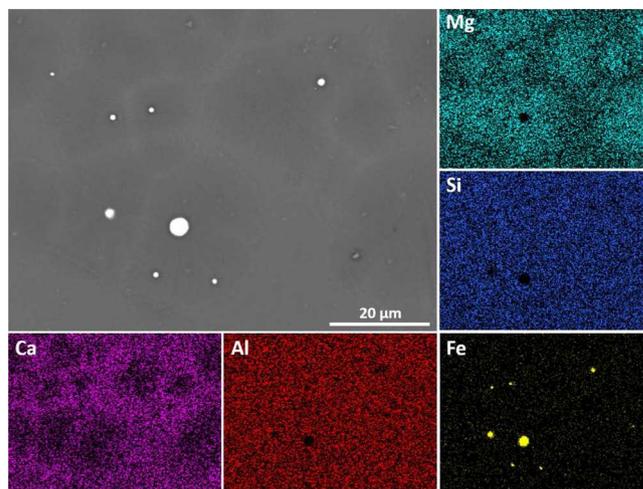


**Fig. 4.** Backscattered electron micrograph and elemental maps of the light region (B) in Trial 1.

composition.

The bulk elemental composition of this glassy material was determined by XRF analysis (Table 3). It comprised, on a molar basis, >86 % $SiO_2$, $Al_2O_3$ and MgO, with 5–6 % CaO and $Na_2O$, and minor contributions from $K_2O$, $TiO_2$ and other elements. Interestingly, $Ce_2O_3$ and $La_2O_3$ were detectable, therefore the added misch metal (as U/Pu simulant) was incorporated into the glassy material rather than partitioning into the metallic portion of these melts (pooling at the bottom of the ICV melts, and not analysed here).

SEM analysis of ground and polished samples (Figs. 3 and 4 & S1−2) reveal that both the light and dark regions exhibit a glassy morphology interspersed with iron/steel droplets. The dark region micrograph (Figs. 3 & S1) revealed a slightly inhomogeneous morphology, with small patches of darker contrast present. With EDX mapping, the glass had a fairly uniform composition, with the exception of droplets of Fe and a number of darker patches, which were somewhat enriched in MgO and lower in CaO than the remainder of the glass.

The light region (B) of Trial 1, was notably less homogeneous than the darker region (A), as shown in the SEM micrographs and EDX maps (Figs. 4 & S2). In addition, much larger dark patches were evident, which were clearly enriched in MgO and deficient in CaO while remaining consistent in $Al_2O_3$ and $SiO_2$. Droplets of Fe were also present, as in the dark region (A), with the dark regions appearing to nucleate
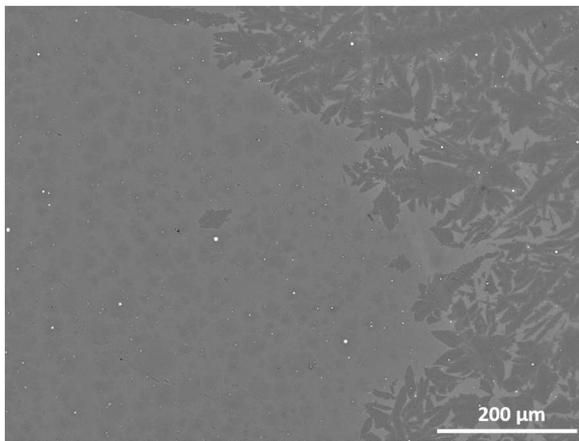
**Fig. 5.** Backscattered electron micrograph of region (B) and (C) interface in Trial 1.
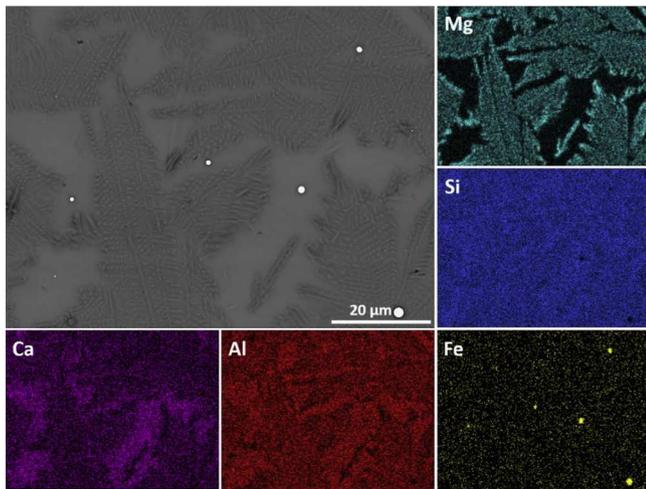


**Fig. 6.** Backscattered electron micrograph and elemental maps of the crystalline region (C) in Trial 1.

**Table 4**
EDX spot analysis of crystalline region (C), (Trial 1) average of 10 spots each. Errors stated are one standard deviation of the 10 measurements.

| Oxide mol. % | Crystals | Glass |
|---|---|---|
| $SiO_2$ | 57.45 ($\pm$ 1.55) | 66.49 ($\pm$ 2.34) |
| MgO | 22.11 ($\pm$ 1.45) | 3.98 ($\pm$ 0.52) |
| $Fe_2O_3$ | 0.04 ($\pm$ 0.05) | 0.09 ($\pm$ 0.18) |
| $Al_2O_3$ | 7.83 ($\pm$ 0.29) | 9.74 ($\pm$ 0.44) |
| CaO | 4.59 ($\pm$ 1.08) | 10.57 ($\pm$ 1.41) |
| $K_2O$ | 0.74 ($\pm$ 0.26) | 0.75 ($\pm$ 0.55) |
| $Na_2O$ | 6.52 ($\pm$ 0.29) | 7.75 ($\pm$ 0.56) |
| MnO | 0.30 ($\pm$ 0.27) | 0.12 ($\pm$ 0.15) |
| $TiO_2$ | 0.41 ($\pm$ 0.20) | 0.51 ($\pm$ 0.35) |

around these droplets. These regions exhibit a crystallite morphology, and may represent some clinoenstatite formation.

Neither the dark nor light regions revealed any hotspots for the rare earth elements added in Trial 1, such as $Ce_2O_3$ and $La_2O_3$ added into the melt via misch metal (maps not shown due to low counts) or any tracer elements. This suggests that these elements were homogeneously incorporated at low concentrations within the material.

The smaller light brown region labelled as "crystalline" (region C) revealed a mass of similar crystallite features across the sample, interspersed with droplets of iron/steel (Fig. 5 & S3). The boundary between
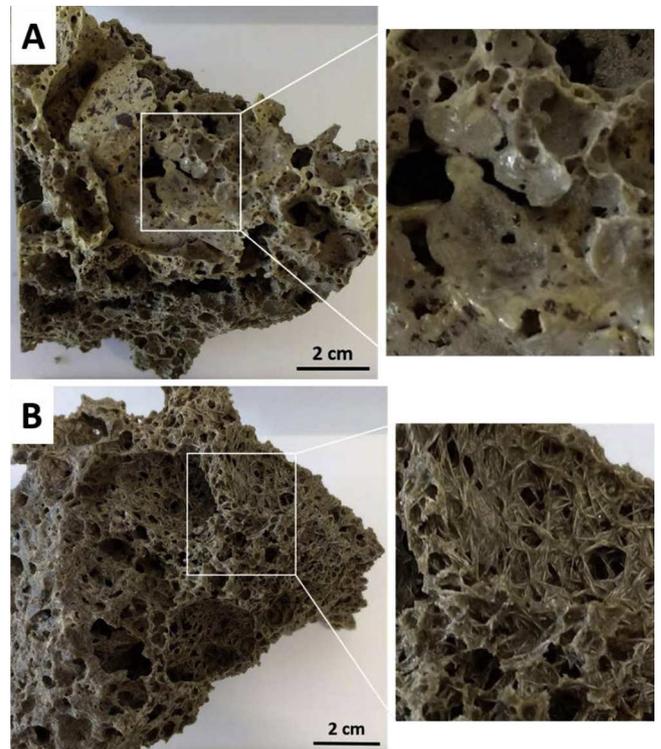


**Fig. 7.** Photograph of Trial 2 glass (A) top, with smooth edges defined as Region 1, (B) underside, exhibiting crystalline masses, defined as Region 2.
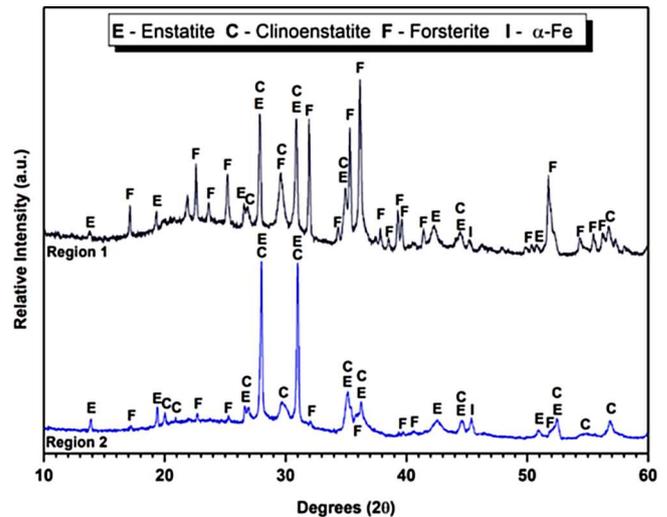


**Fig. 8.** X-ray diffraction patterns of material from Trial 2, Regions 1 and 2.

the crystalline region and the glassy light region was observed to be a sharp transition.

A closer analysis of these crystals with elemental mapping (Fig. 6) revealed a composition that was richer in MgO and deficient in CaO and $Al_2O_3$, when compared to the surrounding glass. EDX spot analysis of the crystals and the glass, shown in Table 4, detail these compositional differences further, in addition to a slight enrichment of MnO in the crystals. As these crystals are interspersed within the glass, there is likely an overlap in EDX measurements and a direct identification of the crystal composition cannot be determined.
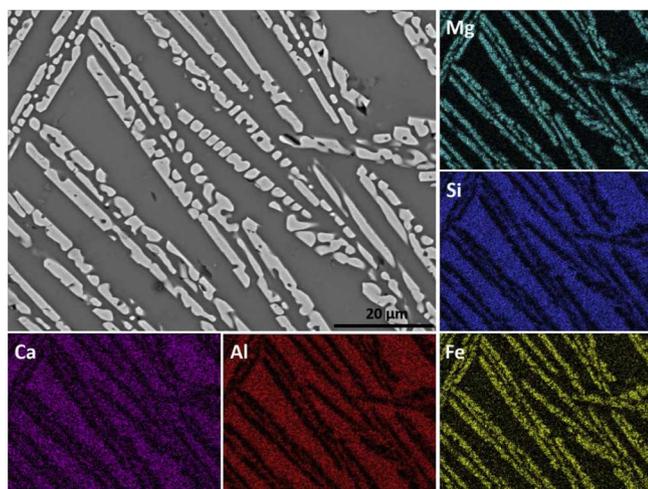
**Fig. 9.** Backscattered electron micrograph and elemental maps of Region 1 in Trial 2.



**Fig. 10.** Backscattered electron micrograph and elemental maps of Region 2 in Trial 2.

**Table 5**

EDX spot measurements for Region 1 – average of 10 measurements for each feature across a high magnification micrograph. Stated error is one standard deviation of the average of 10 measurements.

| Oxide mol. % | Crystals | Glass |
|---|---|---|
| $SiO_2$ | 41.55 (± *1.73*) | 77.56 (± *2.83*) |
| MgO | 42.75 (± *2.30*) | 2.18 (± *0.73*) |
| $Fe_2O_3$ | 13.72 (± *0.91*) | 2.18 (± *0.61*) |
| $Al_2O_3$ | 0.39 (± *0.21*) | 8.25 (± *0.57*) |
| CaO | 0.72 (± *0.29*) | 5.38 (± *1.43*) |
| $K_2O$ | 0.18 (± *0.13*) | 1.45 (± *0.50*) |
| $Na_2O$ | 0.27 (± *0.21*) | 2.38 (± *0.35*) |
| MnO | 0.32 (± *0.37*) | 0.16 (± *0.20*) |
| $TiO_2$ | 0.11 (± *0.13*) | 0.46 (± *0.44*) |

| Element At. % | Crystals | Glass |
|---|---|---|
| Mg / Si | *1.03 (± 0.05)* | *0.03 (± 0.01)* |
| (Mg + Fe) / Si | *1.69 (± 0.10)* | *0.08 (± 0.02)* |
| Mg / Fe | *1.56 (± 0.09)* | *0.50 (± 0.35)* |

### 3.2. Trial 2 – composition and characteristics

The sample from Trial 2 was considerably more heterogeneous than that obtained from Trial 1, with open porosity clearly visible and a combination of both glassy and crystalline features evident (Fig. 7). This is perhaps unsurprising given the location of sampling (from the foam rather than the bulk melt). The Trial 2 melt was divided into two regions of interest, a light beige smooth-sided (Region 1) and a more crystalline side (Region 2). The material used in this study was obtained from the foam layer on top of the melt, and as such, may represent the least durable fraction of the final wasteform, due to the visibly higher surface area.

Analysis of the crystalline phases using XRD (Fig. 8) revealed a combination of forsterite ($Mg_2SiO_4$), enstatite and clinoenstatite (both $MgSiO_3$) within Region 1, along with diffuse scattering indicating the presence of an amorphous component. Due to the iron content of this material (7.25 mol. % $Fe_2O_3$ by XRF oxide analysis, Table 3), these minerals are likely to be iron substituted, falling within the forsterite-fayalite and *(clino)*enstatite-*(clino)*ferrosilite solid solutions.

In Region 2, the relative intensity of the forsterite reflections was significantly reduced compared with those obtained in Region 1, and the dominant phases were identified as enstatite and clinoenstatite (again likely to be Fe substituted) with minor reflections for α–Fe, again alongside some diffuse features corresponding to an amorphous component.
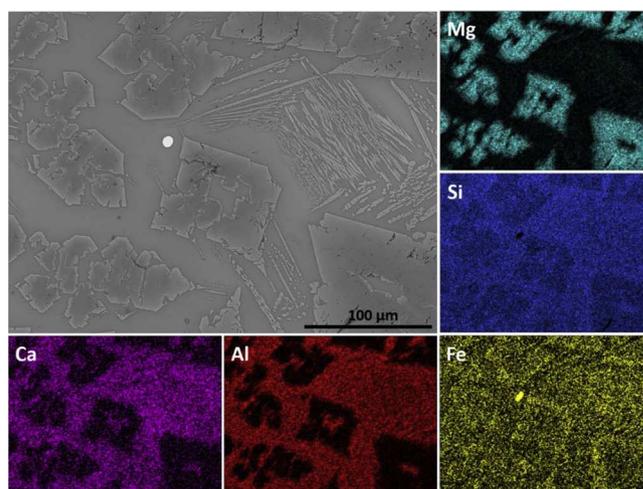
SEM analysis of Region 1 (Figs. 9 & S4) identified one crystalline feature, enriched with MgO and $Fe_2O_3$. The identification of only one crystalline phase appears contrary to XRD data, however, this is considered to be a result of sample preparation; SEM samples for this region were prepared by polishing down the top surface, whilst bulk XRD measurements required powdered material, and it is likely that the sub-surface material has a composition closer to that of Region 2. The major difference in phase assemblage between the two regions is the presence of forsterite, therefore we conclude this surface feature is likely forsterite. Detailed SEM-EDX analysis of Region 1 (Fig. 9 & Table 5) reported quantifiably high MgO and $Fe_2O_3$ contents, with lower $SiO_2$ and much lower concentration for most remaining elements compared to the bulk glass. The (Mg + Fe) / Si ratio of these crystals was found to be 1.7, which is lower than that expected for forsterite (2.0), however due to the thin nature of the crystals, any overlap in EDX measurements with the glass would result in a reduced ratio. The MnO content of the crystals was also observed to be elevated; MnO can substitute into the forsterite structure (with tephroite ($Mn_2SiO_4$) a known end-member). The glass itself was found to be low in alkaline elements and contained 8.25 mol. % $Al_2O_3$. In general, $Al_2O_3$ is known to improve the durability of glass (Hench and Clark, 1978; Chick et al., 1981), though with uncertainty regarding the long-term behaviour of glasses with high $Al_2O_3$ content (Jantzen et al., 2010). The incorporation of MgO within glass (especially in conjunction with $Al_2O_3$) has been linked to enhanced dissolution due to precipitation of magnesium aluminosilicates - an issue of concern for predicting long-term stability of UK HLW glasses containing Mg (Curti et al., 2006; Harrison, 2014; Thien et al., 2012; Narayanasamy et al., 2019; Fisher et al., 2020; Backhouse et al., 2019). The EDX measurements here, however, demonstrate the majority of MgO is bound within crystalline magnesium silicates, with little (2–3 %) incorporated into the glass.

In Region 1, no tracer elements or misch metal components (Ce, La, Nd, Sr, etc.) were identified *via* EDX analysis (Table 5) due to low concentrations. Strong overlap between the principal Sr elemental line (Lα1 1.806 keV) and Si elemental line (Kα1 1.740 keV) rendered Sr detection impossible at these concentrations. Lanthanide quantification relies upon relatively weak Lα1 elemental lines (La 4.647 keV, Ce 4.839 keV and Nd 5.228 keV), which were not significantly above the background signal of the EDX spectra acquired.

Region 2 of Trial 2 was observed to have a multi-phase structure (Fig. 10), comprised of at least two distinct crystalline features embedded within a glassy matrix. The larger crystals appeared to be highly enriched in MgO and slightly elevated in $Fe_2O_3$, with a deficiency of CaO, $Al_2O_3$ and slightly lower $SiO_2$ intensity than the bulk glass. The

**Table 6**
EDX spot analysis of large crystals present within Region 2 of Trial 2 – average of 10 points for each feature across micrograph. Stated error is the standard deviation of the average of 10 points.

| Oxide mol. % | Crystals | Glass |
|---|---|---|
| $SiO_2$ | 52.19 (± 1.29) | 71.98 (± 2.23) |
| MgO | 41.63 (± 1.58) | 2.63 (± 0.55) |
| $Fe_2O_3$ | 4.48 (± 0.44) | 5.41 (± 0.81) |
| $Al_2O_3$ | 0.55 (± 0.26) | 9.29 (± 0.50) |
| CaO | 0.41 (± 0.15) | 6.12 (± 1.55) |
| $K_2O$ | 0.11 (± 0.09) | 1.44 (± 0.22) |
| $Na_2O$ | 0.28 (± 0.22) | 2.67 (± 0.49) |
| MnO | 0.20 (± 0.19) | 0.14 (± 0.17) |
| $TiO_2$ | 0.14 (± 0.14) | 0.32 (± 0.33) |

| Element At. % | Crystals | Glass |
|---|---|---|
| Mg / Si | 0.80 | 0.04 |
| (Mg + Fe) / Si | 0.97 | 0.19 |
| Mg / Fe | 4.60 | 0.24 |
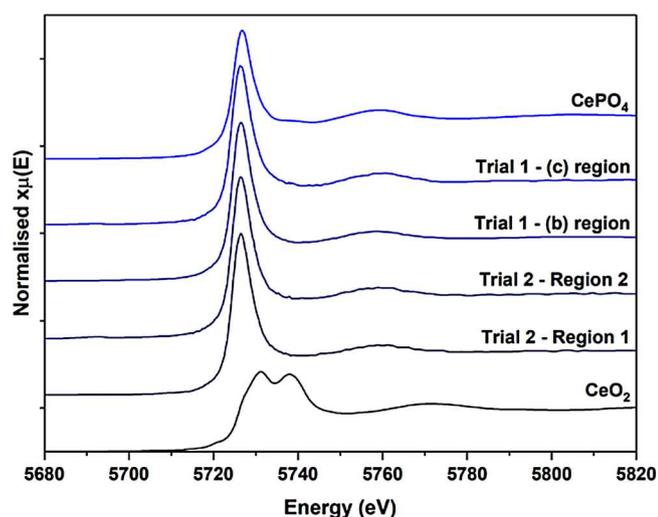


**Fig. 11.** Ce $L_3$ edge XANES data for the two major Regions identified within each trial, compared with data acquired for $CeO_2$ ($Ce^{4+}$ reference compound) and $CePO_4$ ($Ce^{3+}$ reference compound).

(Mg + Fe) / Si ratio for Region 2 (Table 6) was close to 1.0, suggesting the formation of an Fe-substituted (clino-)enstatite ($MgSiO_3$). The composition of the lighter, thinner crystals (≤10 μm) was not obtainable, since they were too thin to individually spot map without significant overlap from the glass phase in which they were embedded, however it is clear that the mass of thin crystals slightly enriched in MgO and $Fe_2O_3$ (Fig. 10). As in Region 1, the glass composition for Region 2 was found to be relatively low in soluble alkali elements, and contained roughly the same level of $Al_2O_3$ at 9.29 ± 0.50 mol. %.

### 3.3. Ce $L_3$ XANES analysis

The crystalline phases identified via XRD for both these trials were magnesium-iron silicates within the olivine or pyroxene groups. The elements added as radionuclide simulants (such as Ce, La, Sr, Nd) have larger ionic radii than the structural elements of these crystals, which makes incorporation unlikely. Studies on crystallisation from melts in olivines and pyroxenes consistently show very low partitioning coefficients for these elements (Kennedy et al., 1993; Beattie, 1994), which also extends to U (Kennedy et al., 1993; Beattie, 1994; Blundy and Wood, 2003). This points towards these elements being incorporated within the glassy phase of these vitreous materials.

Understanding the local environment conditions of the radionuclide simulant elements is important for understanding the durability of these

vitreous materials, and for predicting the chemistry of U, Pu within these systems if these melts were to be produced using real active wastes. To assist with this, the speciation of Ce within both these trials was determined by investigation of Ce $L_3$ edge XANES (Fig. 11).

The Ce absorption edge and distinct XANES features allow comparison with $CePO_4$ (monazite, as $Ce^{3+}$) and $CeO_2$ (as $Ce^{4+}$). The singular strong feature at 5725.9 eV for $Ce^{3+}$ in the XANES of the $CePO_4$ reference compound is identical to that observed for the vitrified materials. In contrast, the two features at slightly higher energies (5729.5 eV and 5737.8 eV) observed for $Ce^{4+}$ in the $CeO_2$ reference compound, are not apparent within the data of the vitrified products. These data indicate the Ce present within the vitreous product is as $Ce^{3+}$. Although this indicates that the misch metal was incorporated into the product, the presence of $Ce^{3+}$ only suggests that the overall melt conditions were reducing, as Ce containing glasses often contain both $Ce^{3+}/Ce^{4+}$ unless reducing conditions are imposed (Darab et al., 1998; Larson et al., 1990; Curti et al., 2012). This is similar Ce speciation identified in previous PCM simulant vitrification (Hyatt et al., 2014), and indicates any Pu may also be retained within a $Pu^{3+}$ environment.

### 3.4. Durability assessment

One aspect of the disposability of these vitreous materials, their bulk aqueous durability, was assessed using static leach testing protocol, utilising Type I water, according to ASTM C1285 (PCT-B) over a 28 d period at 90 °C. The normalised mass loss for the major structural elements within the glasses, along with pH, are shown in Fig. 12.

At 1 d of leaching, the pH of the solutions increased to 9.7 and 8.8 (± 0.1), respectively, for Trial 1 and Trial 2. After this time, the pH remained essentially consistent over the 28 d testing period, with final pH values of 9.9 and 9.1 (± 0.1) for Trial 1 and Trial 2, respectively. The slightly elevated pH of the glass in Trial 1 compared with Trial 2 was expected, given the variation in readily soluble alkali elements between the trials (Trial 1: $Na_2O$ + $K_2O$ = 6.74 mol. %, Trial 2: $Na_2O$ + $K_2O$ = 2.17 mol. %, along with a higher CaO content in Trial 1).

Most high level waste glass materials contain B, which is often used as a 'tracer' for glass dissolution since it does not participate in the formation of passivating layers or secondary precipitates. There was no B added to the glass melts investigated here, therefore Na was used to trace the dissolution of the glass, since its release to solution is generally concurrent with the breakdown of the glass structure. It is known to form secondary phases, but typically only in high pH solutions (>pH 10) (Mann et al., 2019; Fournier et al., 2019). After 28 d of leaching, the $NL_{Na}$ was 0.26 ± 0.01 g/m² for Trial 1 and 0.51 ± 0.02 g/m² for Trial 2. This is contradictory to the pH measurements; Si solubility is greater at high pH, therefore it should be expected that the glass in Trial 1, which exhibited a higher pH, should dissolve more than that from Trial 2. The residual dissolution rates (Table 7) of Na were also higher for Trial 2 than Trial 1 (7.84 × 10⁻³ g/m²/d compared with 4.06 × 10⁻³ g/m²/d, respectively).

Glasses that contain significant proportions of Mg are known to dissolve at relatively rapid rates, due to the low $\Delta G_{hyd}$ of Mg, favouring the rapid precipitation of Mg-bearing (alumino)silicate hydrate minerals such as phyllosilicate clays (Backhouse et al., 2019), which, in turn drives further Si dissolution from the glass, elevating dissolution rates. Fig. 12 shows that although the Mg normalised mass loss was low for both glasses, it significantly decreased with time. This decrease was more pronounced for the glass from Trial 1 than Trial 2, suggesting that Mg-(alumino)silicate hydrate secondary phase formation may have been greatest for this glass. Again, from this observation, one might expect the dissolution rate of the glass in Trial 1 to be faster than those in Trial 2, however the opposite trend was observed.

The $NL_{Ca}$ initially increased and then began to decrease for both glasses. Throughout the experiment, the $NL_{Ca}$ was lower for the glass in Trial 1 than in Trial 2. Calcium is known to have a strong affinity for silica within the passivating layer formed at the surface of dissolving
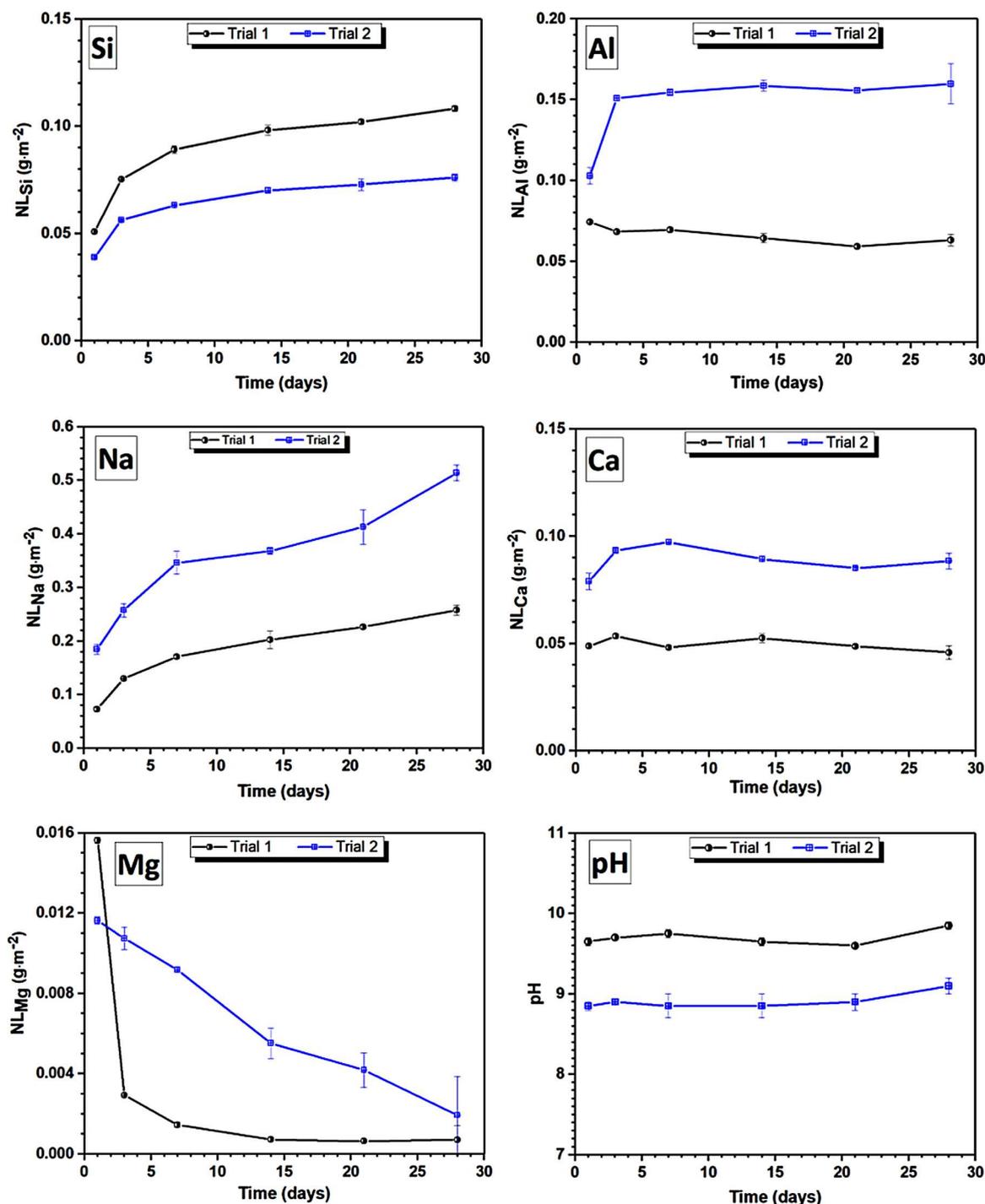
**Fig. 12.** Normalised elemental mass losses (NL$_i$) for Si, Al, Na, Ca and Mg along with pH measurements from PCT-B durability assessments for both Trial 1 and Trial 2 glasses, over a 28 d period.

**Table 7**
Normalised release rates for Na and Si for each of the glass compositions.

| NR (g·m$^{-2}$·d$^{-1}$) | | Initial rate (0−7 d) | Residual rate (7−28 d) |
|---|---|---|---|
| Trial 1 | Na | $1.55 \times 10^{-2} \pm 4.46 \times 10^{-3}$ | $4.06 \times 10^{-3} \pm 1.56 \times 10^{-4}$ |
| | Si | $5.97 \times 10^{-3} \pm 2.18 \times 10^{-3}$ | $8.74 \times 10^{-4} \pm 1.00 \times 10^{-4}$ |
| Trial 2 | Na | $2.62 \times 10^{-2} \pm 3.53 \times 10^{-3}$ | $7.84 \times 10^{-3} \pm 1.81 \times 10^{-3}$ |
| | Si | $3.72 \times 10^{-3} \pm 1.72 \times 10^{-3}$ | $5.92 \times 10^{-4} \pm 9.55 \times 10^{-5}$ |

glass; glasses which incorporate Ca into the silica gel demonstrate significantly lower dissolution rates than those without Ca (Corkhill et al., 2013; Aréna et al., 2019; Utton et al., 2012). This is the likely explanation for why the dissolution rate of the Glass in Trial 1 was lower than that of Trial 2, despite the higher pH and removal of Mg from solution. Notwithstanding these observations, the dissolution rates of both glasses are within the same order of magnitude, despite the different compositions and processing conditions.

The normalised mass loss of elements were compared with those for UK high level waste glass, which is destined for disposal within a geological disposal facility. Though not the same composition, and not
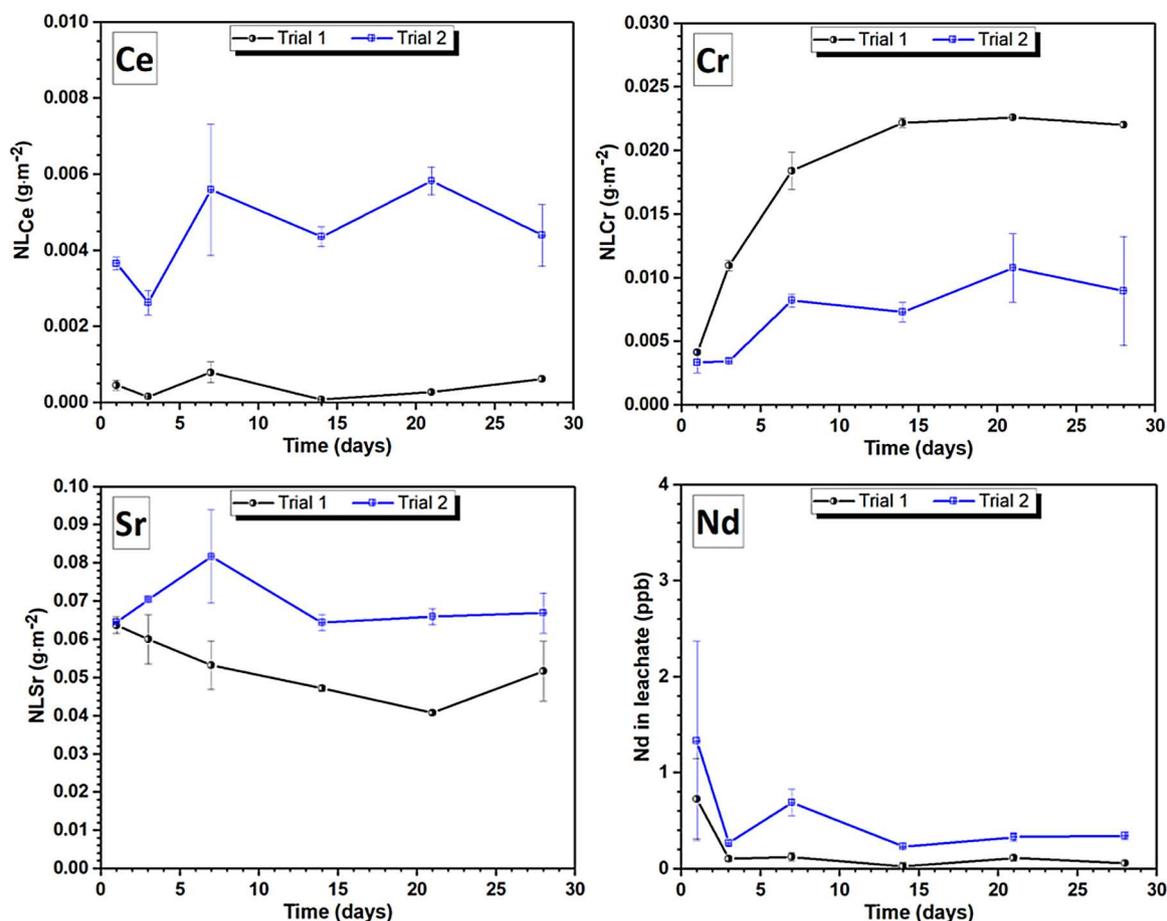
**Fig. 13.** Normalised elemental mass losses ($NL_i$) for Ce, Cr and Sr, and concentrations of Nd from PCT-B durability assessments for both Trial 1 and Trial 2 glasses, over a 28 d period.

destined for use with the same wastes, these glasses provide some of the largest datasets of UK waste simulant glasses. The glasses investigated in the current study had $NL_{Na}$ and $NL_{Si}$ values that were an order of magnitude lower than those reported for 25 wt. % and 38 wt. % loaded MW glass (Harrison, 2014) tested at 90 °C, and comparable to the newly formulated Ca/Zn-MW high level waste glass with a 28 wt. % waste loading tested at 50 °C (Fisher et al., 2020) (which will result in a much lower release than with higher temperature leaching).

The normalised mass loss of surrogate radionuclide elements incorporated within the glasses are shown in Fig. 13. The $NL_{Sr}$ was similar to that of $NL_{Ca}$ (Fig. 12), which is expected given the chemical similarity between the elements; the maximum normalised mass loss of Sr was < 0.1 g·m$^{-2}$. As with the $NL_{Ca}$, the $NL_{Sr}$ was lower for the glass in Trial 1 than Trial 2, suggesting that it may be incorporated with Ca into the silica gel layer. The release of lanthanide elements was extremely low over the 28 d period, with the normalised mass loss of Ce (as a surrogate for Pu) reaching a maximum of $0.0008 \pm 0.0002$ g·m$^{-2}$ and $0.0058 \pm 0.0004$ g·m$^{-2}$ for Trials 1 and 2 respectively. Very low concentrations of Nd were also detected in solution, however, normalised rates cannot be calculated due to lack of XRF data for this element (for normalisation). As such, only concentration values are shown in Fig. 13.

## 4. Conclusions

The materials characterised in this study were produced through in-container vitrification of UK simulant wastes, combined with glass forming additives. The resultant vitreous wasteforms were heterogeneous in nature, predominately forming olivine and pyroxene group magnesium-iron silicate minerals, dispersed throughout a glassy matrix.

The bulk glasses were found to consist of moderately low alkali NaO-CaO-Al$_2$O$_3$-(Fe$_2$O$_3$)-SiO$_2$ systems, with a degree of MgO incorporation. Spatially resolved compositional data and oxidation state analysis point towards Pu surrogate elements and other tracer elements partitioning into the glassy phase. Both materials (from Trial 1 and Trial 2) performed adequately during the 28 d durability assessment, with major elemental release being one order of magnitude lower than for UK HLW waste glasses, and with very low release rates for the Pu surrogate Ce. The characteristics and durability of these materials is especially notable considering these were trial materials, with additives/wastes that were not optimised for improving wasteform performance. Overall, the characterisation and durability testing of these two materials indicate that the GeoMelt trials, and the in-container vitrification technology itself, could produce wasteforms which exceed the dissolution performance of current UK HLW glass formulations, under similar conditions.

## CRediT authorship contribution statement

**Sam A. Walling:** Methodology, Formal analysis, Investigation, Writing - original draft, Visualization. **Marcus N. Kauffmann:** Investigation, Writing - review & editing, Visualization. **Laura J. Gardner:** Methodology, Investigation, Writing - review & editing. **Daniel J. Bailey:** Methodology, Investigation, Writing - review & editing. **Martin C. Stennett:** Methodology, Formal analysis, Investigation, Visualization. **Claire L. Corkhill:** Writing - review & editing, Supervision. **Neil C. Hyatt:** Conceptualization, Methodology, Investigation, Writing - review & editing, Supervision, Funding acquisition.

## Declaration of Competing Interest

The authors report no declarations of competing interest.

## Acknowledgements

## Appendix A. Supplementary data

Supplementary material related to this article can be found, in the online version, at doi:https://doi.org/10.1016/j.jhazmat.2020.123764.

## References

Aréna, H., Rébiscoul, D., Garcès, E., Godon, N., 2019. Comparative effect of alkaline elements and calcium on alteration of International Simple Glass. Npj Mater. Degrad. 3 (1), 10.

Backhouse, D.J., Corkhill, C.L., Hyatt, N.C., Hand, R.J., 2019. Investigation of the role of Mg and Ca in the structure and durability of aluminoborosilicate glass. J. Non-Cryst. Solids 512, 41–52.

Beattie, P., 1994. Systematics and energetics of trace-element partitioning between olivine and silicate melts: implications for the nature of mineral/melt partitioning. Chem. Geol. 117 (1), 57–71.

Bennett, D.G., Higgo, J.J.W., Wickham, S.M., 2001. Review of Waste Immobilisation Matrices. United Kingdom Nirex Limited.

Bingham, P.A., Hyatt, N.C., Hand, R.J., 2012. Vitrification of UK intermediate level radioactive wastes arising from site decommissioning: property modelling and selection of candidate host glass compositions. Glass Technol. Eur. J. Glass Sci. Technol. Part A 53 (3), 83–100.

Blundy, J., Wood, B., 2003. Mineral-melt partitioning of uranium, thorium and their daughters. Rev. Mineral. Geochem. 52 (1), 59–123.

Bradshaw, K., Gribble, N.R., Hughes, D.O., Riley, A.D., 2007. UK full-scale Non-active vitrification development and implementation of research findings onto the waste vitrification plant. In: WM'07 Conference. Tucson, AZ.

Campbell, P., Witwer, K., Finucane, K., Ohl, P., Scales, C., 2016. Status update - installation and operation of geomelt ICV process in the NNL Central Laboratory on the Sellafield Site. In: WM2016 Conference. Phoenix, AZ.

Campbell, B., Dysland, E.J., Finucane, K.G., Hatt, S., Moulin-Ramsden, M.G., Woosley, S.L., Scales, C.R., Roe, J.I., 2017. Commissioning of a GeoMelt vitrification plant at the central laboratory on the Sellafield site. In: WM2017 Conference. Phoenix, AZ.

Chen, T.-Y., Maddrell, E.R., Hyatt, N.C., Gandy, A.S., Stennett, M.C., Hriljac, J.A., 2018. Transformation of Cs-IONSIV® into a ceramic wasteform by hot isostatic pressing. J. Nucl. Mater. 498, 33–43.

Chick, L.A., Piepel, G.F., Mellinger, G.B., May, R.P., Gray, W.J., Buckwalter, C.Q., 1981. Effects of Composition on Properties in an 11-Component Nuclear Waste Glass System, United States, p. 120.

Clarke, S., Scales, C., Patel, N., Roe, J., Banford, A.W., 2020. Active demonstration of the thermal treatment of surrogate sludge and surrogate drums using the GeoMelt™ in container vitrification (ICV) melter installed in NNL Central laboratory. IOP Conference Series: Materials Science and Engineering 818, 012004.

Corkhill, C.L., Cassingham, N.J., Heath, P.G., Hyatt, N.C., 2013. Dissolution of UK high-level waste glass under simulated hyperalkaline conditions of a colocated geological disposal system. Int. J. Appl. Glass Sci. 4 (4), 341–356.

Cronin, J., Collier, N., 2011. Corrosion & Expansion of Grouted Magnox. NDA.

Curti, E., Crovisier, J.L., Morvan, G., Karpoff, A.M., 2006. Long-term corrosion of two nuclear waste reference glasses (MW and SON68): a kinetic and mineral alteration study. Appl. Geochem. 21 (7), 1152–1168.

Curti, E., Grolimund, D., Borca, C.N., 2012. A micro-XAS/XRF and thermodynamic study of CeIII/IV speciation after long-term aqueous alteration of simulated nuclear waste glass: Relevance for predicting Pu behavior? Appl. Geochem. 27 (1), 56–63.

Darab, J.G., Li, H., Vienna, J.D., 1998. X-ray absorption spectroscopic investigation of the environment of cerium in glasses based on complex cerium alkali borosilicate compositions. J. Non-Cryst. Solids 226 (1), 162–174.

Deckers, J., 2011. Treatment of low-level radioactive waste by plasma: a proven technology? ASME 2010 13th International Conference on Environmental Remediation and Radioactive Waste Management 247–251.

Dunnett, B.F., 2007. Review of Development of UK High Level Waste Vitrified Product. Nexia Solutions.

Fairhall, G.A., Palmer, J.D., 1992. The encapsulation of magnox swarf in cement in the United Kingdom. Cem. Concr. Res. 22 (2–3), 293–298.

Fenton, A., Holland, T.R., 2001. The History and Expected Benefits of using Cemented Materials for the Encapsulation of Radioactive Waste in the UK. AEA Technology.

Finucane, K., Campbell, B., 2006. The treatment of mixed waste with GeoMelt in-container vitrification. In: WM'06 Conference. Tucson, AZ.

Finucane, K., Thompson, L.E., Abuku, T., Nakauchi, H., 2008. Treatment of asbestos wastes using the GeoMelt vitrification process. In: WM2008 Conference. Phoenix, AZ.

Fisher, A.J., Imran, M.N.B., Mann, C., Gausse, C., Hand, R.J., Hyatt, N.C., Corkhill, C.L., 2020. Short communication: the dissolution of UK simulant vitrified high-level-waste in groundwater solutions. J. Nucl. Mater., 152245. In Press.

Fournier, M., Ducasse, T., Pérez, A., Barchouchi, A., Daval, D., Gin, S., 2019. Effect of pH on the stability of passivating gel layers formed on International Simple Glass. J. Nucl. Mater. 524, 21–38.

Garrett, B., Campbell, B., Finucane, K., Woosley, S., Gaither, B., Mitchell, R., Miklos, R., Connolly, M., Butler, S., 2020. Treatment of problematic reactive metal wastes using the GeoMelt in-container vitrification (ICV™) process. In: WM2020 Conference. Phoenix, AZ.

Gin, S., Abdelouas, A., Criscenti, L.J., Ebert, W.L., Ferrand, K., Geisler, T., Harrison, M.T., Inagaki, Y., Mitsui, S., Mueller, K.T., Marra, J.C., Pantano, C.G., Pierce, E.M., Ryan, J.V., Schofield, J.M., Steefel, C.I., Vienna, J.D., 2013. An international initiative on long-term behavior of high-level nuclear waste glass. Mater. Today 16 (6), 243–248.

Goel, A., McCloy, J.S., Pokorny, R., Kruger, A.A., 2019. Challenges with vitrification of Hanford High-Level Waste (HLW) to borosilicate glass – an overview. J. Non-Crystalline Solids: X 4, 100033.

Harrison, M.T., 2014. The effect of composition on short- and long-term durability of UK HLW glass. Proc. Mater. Sci. 7, 186–192.

Heath, P.G., Stewart, M.W.A., Moricca, S., Hyatt, N.C., 2018. Hot-isostatically pressed wasteforms for Magnox sludge immobilisation. J. Nucl. Mater. 499, 233–241.

Heep, W., 2011. The zwilag plasma facility: Five years of successful operation. ASME 2010 13th International Conference on Environmental Remediation and Radioactive Waste Management 141–147.

Hench, L.L., Clark, D.E., 1978. Physical chemistry of glass surfaces. J. Non-Cryst. Solids 28 (1), 83–105.

Hujova, M., Klouzek, J., Cutforth, D., Lee, S., Miller, M., Kruger, A., Hrma, P., Pokorny, R., 2020. Feed-to-glass conversion during low activity waste vitrification. Ceram. Int. 46 (7), 9826–9833.

Hyatt, N.C., Schwarz, R.R., Bingham, P.A., Stennett, M.C., Corkhill, C.L., Heath, P.G., Hand, R.J., James, M., Pearson, A., Morgan, S., 2014. Thermal treatment of simulant plutonium contaminated materials from the Sellafield site by vitrification in a blast-furnace slag. J. Nucl. Mater. 444 (1), 186–199.

Hyatt, N.C., Corkhill, C.L., Stennett, M.C., Hand, R.J., Gardner, L.J., Thorpe, C.L., 2020. The HADES facility for high activity decommissioning engineering & science: part of the UK National Nuclear User Facility. IOP Conference Series: Materials Science and Engineering 818, 012022.

Jantzen, C.M., Ojovan, M.I., 2019. On selection of matrix (Wasteform) material for higher activity nuclear waste immobilization (review). Russ. J. Inorg. Chem. 64 (13), 1611–1624.

Jantzen, C.M., Brown, K.G., Pickett, J.B., 2010. Durable glass for thousands of years. Int. J. Appl. Glass Sci. 1 (1), 38–62.

Kennedy, A.K., Lofgren, G.E., Wasserburg, G.J., 1993. An experimental study of trace element partitioning between olivine, orthopyroxene and melt in chondrules: equilibrium values and kinetic effects. Earth Planet. Sci. Lett. 115 (1), 177–195.

Kim, D., 2015. Glass property models, constraints, and formulation approaches for vitrification of high-level nuclear wastes at the US hanford site. J. Korean Ceram. Soc 52 (2), 92-0.

Kim, M., Kim, H.G., Kim, S., Yoon, J.-H., Sung, J.Y., Jin, J.S., Lee, M.-H., Kim, C.-W., Heo, J., Hong, K.-S., 2020. Leaching behaviors and mechanisms of vitrified forms for the low-level radioactive solid wastes. J. Hazard. Mater. 384, 121296.

Larson, E.M., Lytle, F.W., Eller, P.G., Greegor, R.B., Eastman, M.P., 1990. XAS study of lanthanide ion speciation in borosilicate glass. J. Non-Cryst. Solids 116 (1), 57–62.

Laverov, N.P., Omel'yanenko, B.I., Yudintsev, S.V., Stefanovsky, S.V., Nikonov, B.S., 2013. Glasses for immobilization of low- and intermediate-level radioactive waste. Geol. Ore Depos. 55 (2), 71–95.

Mann, C., Ferrand, K., Liu, S., Eskelsen, J.R., Pierce, E., Lemmens, K., Corkhill, C., 2019. Influence of young cement water on the corrosion of the International Simple Glass. Npj Mater. Degrad. 3 (1), 5.

Narayanasamy, S., Jollivet, P., Godon, N., Angeli, F., Gin, S., Cabié, M., Cambedouzou, J., Le Guillou, C., Abdelouas, A., 2019. Influence of composition of nuclear waste glasses on vapor phase hydration. J. Nucl. Mater. 525, 53–71.

Nieminen, M., Olin, M., Laatikainen-Lutama, J., Wickham, S.M., Doudou, S., Fuller, A.J., Kent, J., Fournier, M., Clarke, S., Scales, C., Hyatt, N.C., Walling, S.A., Gardner, L.J., Catherin, S., Frasca, B., 2019. Thermal treatment for radioactive waste minimisation. EPJ Nuclear Sci. Technol. 6 (25).

Nuclear Decommissioning Authority, 2010. Plutonium: Credible Options Analysis. NDA.

Nuclear Decommissioning Authority, 2015. NDA Higher Activity Waste Treatment Framework. NDA.

Nuclear Decommissioning Authority, 2016. Integrated Waste Management: NDA Higher Activity Waste Strategy. NDA.

Nuclear Decomissioning Authority, 2018. Integrated Waste Management - Radioactive Waste Strategy. NDA.

Nuclear Decomissioning Authority, 2019. 2019 UK Radioactive Waste and Material Inventory: Radioactive Waste Inventory. NDA.

Nuclear Decomissioning Authority, 2019. Waste Stream 2F02: Plutonium Contaminated Materials; Drums. NDA.

Nuclear Decomissioning Authority, 2019. Waste Stream 2F34: Plutonium Contaminated Materials; Drums. NDA.

Nuclear Decomissioning Authority, 2019. Waste Stream 7A21: Operational ILW Plutonium Contaminated. NDA.

Nuclear Decomissioning Authority, 2019. Waste Stream 7A111: Decommissioning Waste PCM ILW. NDA.

Nuclear Decomissioning Authority, 2019. Waste Stream 2D90: Plutonium Contaminated Materials; Drums. NDA.

Nuclear Decomissioning Authority, 2019. Waste Stream 2D34: Sludge From Sand Filters and Transfers. NDA.

Nuclear Decomissioning Authority, 2019. Waste Stream 2D08.1: MSSS Compartment 1. NDA.

Nuclear Decomissioning Authority, 2019. Waste Stream 2D07: Pile Fuel Cladding and Miscellaneous Solid Waste. NDA.

Nuclear Decomissioning Authority, 2019. Waste Stream 2D26: Ion Exchange Material (Clinoptilolite) and Sand. NDA.

Ojovan, M.I., Lee, W.E., 2011. Glassy wasteforms for nuclear waste immobilization. Metall. Mater. Trans. A 42 (4), 837–851.

Radioactive Waste Management (RWM), 2017. Geological Disposal: Review of Alternative Radioactive Waste Management Options. RWM.

Ravel, B., Newville, M., 2005. ATHENA, ARTEMIS, HEPHAESTUS: data analysis for X-ray absorption spectroscopy using IFEFFIT. J. Synchrotron Radiat. 12, 537–541.

Robbins, R.A., Ojovan, M.I., 2016. Vitreous materials for nuclear waste immobilisation and IAEA support activities. MRS Adv. 1 (63–64), 4201–4206.

Scourfield, S.J., Kent, J.E., Wickham, S.M., Nieminen, M., Clarke, S., Frasca, B., 2020. Thermal treatment for radioactive waste minimisation and hazard reduction: overview and summary of the the EC THERAMIN project. IOP Conference Series: Materials Science and Engineering 818, 012001.

Setiadi, A., Milestone, N.B., Hill, J., Hayes, M., 2006. Corrosion of aluminium and magnesium in BFS composite cements. Adv. Appl. Ceram. 105 (4), 191–196.

Sharp, J.H., Hill, J., Milestone, N.B., Miller, E.W., 2003. Cementitious systems for encapsualation of intermediate level waste. ASME Conference Proceedings (37327) 1425–1433.

Shu, X., Li, Y., Huang, W., Chen, S., Xu, C., Zhang, S., Li, B., Wang, X., Qing, Q., Lu, X., 2020. Rapid vitrification of uranium-contaminated soil: effect and mechanism. Environ. Pollut. 263, 114539.

Thien, B.M.J., Godon, N., Ballestero, A., Gin, S., Ayral, A., 2012. The dual effect of Mg on the long-term alteration rate of AVM nuclear waste glasses. J. Nucl. Mater. 427 (1), 297–310.

Thompson, L.E., 2002. Results and reaction mechanism for the treatment of concentrated chlorinated organics using GeoMelt vitrification. In: Third International Conference on Remediation of Chlorinated and Recalcitrant Compounds. Monterey, CA.

Thornber, S.M., Stennett, M.C., Vance, E.R., Chavara, D.T., Watson, I., Jovanovic, M., Davis, J., Gregg, D., Hyatt, N.C., 2018. A preliminary validation study of PuO$_2$ incorporation into zirconolite glass-ceramics. MRS Adv. 3 (20), 1065–1071.

Utton, C., Godfrey, I., 2010. Review of Stability of Cemented Grouted Ion-Exchange Materials, Sludges and Flocs. NNL.

Utton, C.A., Swanton, S.W., Schofield, J., Hand, R.J., Clacher, A., Hyatt, N.C., 2012. Chemical durability of vitrified wasteforms: effects of pH and solution composition. Mineral. Mag. 76 (8), 2919–2930.

Vienna, J.D., 2010. Nuclear waste vitrification in the United States: recent developments and future options. Int. J. Appl. Glass Sci. 1 (3), 309–321.

Witwer, K., Dysland, E., 2010. Thermal treatment of UK intermediate and low level radioactive waste: a demostration of the GeoMelth process towards treatment of Sellafield waste. In: WM2010 Conference. Phoenix, AZ.

Witwer, K.S., Woolery, D.W., Dysland, E.J., 2006. Progress on the Hanford bulk vitrification project ICV$^{TM}$ testing program. In: WM'06 Conference. Tucson, AZ.

Witwer, K.S., Dysland, E.J., Garfield, J.S., Beck, T.H., Matyas, J., Bagaasen, L.M., Cooley, S.K., Pierce, E., Kim, D.-S., Schweiger, M.J., 2008. Hanford's supplemental treatment project: full-scale integrated testing of in-container-vitrification and a 10,000-liter dryer. In: WM2008 Conference. Phoenix, AZ.

Witwer, K., Woosley, S., Campbell, B., 2013. Geomelt ICV treatment of Sellafield pond solids waste. In: WM2013 Conference. Phoenix, AZ.

Zhang, S., Shu, X., Chen, S., Yang, H., Hou, C., Mao, X., Chi, F., Song, M., Lu, X., 2017. Rapid immobilization of simulated radioactive soil waste by microwave sintering. J. Hazard. Mater. 337, 20–26.